https://doi.org/10.5194/egusphere-2026-969
Preprint. Discussion started: 26 February 2026

Shifts in the Dominance of Climatic, Anthropogenic, and Landscape Drivers Explain the Spatial Variation in the Budyko-type Equation Parameter

Bingbing Ding[1], Dandan Wang[2], Guodong Jia[3,4], Xinxiao Yu[3,4], Yan Li[1]

[1]College of forestry and biotechnology, Zhejiang A&F University, Hangzhou, China
[2]Institute of Sediment Research, China Institute of Water Resources and Hydropower Research, Beijing, China
[3]The Metropolitan Area Forest Ecosystem Research Station, School of Soil and Water Conservation, Beijing Forestry University, Beijing, China
[4]Key Laboratory of State Forestry and Grassland Administration on Soil and Water Conservation, Beijing Forestry University, Beijing, China

Correspondence to: Guodong Jia (jgd3bjfu@163.com); Xinxiao Yu(yuxinxiao111bjfu@163.com)

Abstract. Hydroclimatic transition zones are critical hotspots of global environmental change, yet the spatial heterogeneity of their hydrological functioning remains poorly understood because of the complex interplay of natural and anthropogenic factors. In this study, we propose a machine learning-driven diagnostic framework to better understand the spatially divergent drivers of the Budyko parameter (ω) across 12 representative catchments in the semi-arid to semi-humid transition zone. By integrating principal component analysis with hierarchical clustering, we objectively identified three distinct hydrological functional zones. Four machine learning algorithms (XGBoost, RF, ANN, and SVM) were subsequently systematically benchmarked for each zone to select the optimal model, and Shapley Additive exPlanations (SHAP) analysis was performed to quantify the driving mechanisms. The results reveal a fundamental spatial shift in the dominant drivers of ω: C1 is dominated by climatic factors (53.52%), C3 is dominated by anthropogenic factors (68.73%), and C2 is jointly driven by climatic (37.24%), anthropogenic (31.85%), and landscape (30.91%) factors. Specifically, the primary drivers for ω are temperature (T, 32.42%) in C1, leaf area index (LAI, 24.59%) in C2, and GDP (25.09%) in C3. The critical thresholds for shifting the directional contribution of these factors were 8.17 ℃, 1.16, and 25.8×10^4 USD, respectively. Furthermore, the directional impacts of climatic, anthropogenic, and landscape drivers vary significantly across zones, with pairwise interactions exhibiting distinct patterns of synergy and trade-offs. This study demonstrates that local landscape characteristics and human activity patterns can override macroclimatic controls, providing support for spatially differentiated water resource management in climatic transition zones.

1 Introduction

Water availability in climatic transition zones—spanning from semi-arid to semi-humid regions—represents one of the most volatile components of the global terrestrial water cycle (Huang et al., 2016; Seneviratne et al., 2010). Unlike humid regions, which are controlled by energy, or arid regions, which are controlled by water supply, these transitional environments are in delicate equilibrium and exhibit high sensitivity to both climate variability and land surface changes (Koster et al., 2004;

https://doi.org/10.5194/egusphere-2026-969
Preprint. Discussion started: 26 February 2026

Berghuijs et al., 2014). In the Anthropocene, this complexity is further exacerbated by intensive anthropogenic activities. As population pressure and food demand increase, these transition zones have emerged as hotspots of "socio-hydrological" coevolution (Sivapalan et al., 2012). Here, natural hydrological signals are not merely superimposed by anthropogenic activities but are often fundamentally reshaped by extensive landscape modifications—such as agricultural expansion, urbanization, and ecological engineering—and intensive water resource exploitation (Sterling et al., 2013; Vörösmarty et al., 2010)). This intense coupling creates a nonstationary environment where the dominant drivers of runoff change may shift dynamically over space and time, rendering traditional stationary assumptions invalid (Milly et al., 2008). Therefore, quantitatively attributing the drivers of runoff change and identifying their shifting dominance in these complex transition zones is critical for predicting future water security and developing adaptive management strategies (Zhai and Tao, 2017; Yang et al., 2014).

To quantitatively decode these complex interactions, current methodologies primarily include process-based hydrological modeling, statistical analysis, and Budyko water–energy balance approaches (Duveiller et al., 2018; Ding et al., 2025; Dey and Mishra, 2017)). While process-based models capture detailed physical mechanisms, they are often hindered by parameter uncertainty and structural complexity (Rajib et al., 2016; Yin et al., 2017). Statistical methods, although intuitive, typically lack physical interpretability (Ni et al., 2022; Xu et al., 2014). In contrast, the Budyko framework stands out for its elegant balance between physical soundness and computational parsimony, making it a robust theoretical lens for disentangling the drivers of hydrological change (Xu et al., 2014; Duveiller et al., 2018; Budyko and Miller, 1974). Within this framework, the long-term partitioning of precipitation into evapotranspiration and runoff is governed by the supply–demand balance of water and energy. This relationship is mathematically formalized by widely recognized analytical solutions, such as the Fu equation (Fu, 1981) and the Choudhury–Yang equation (Yang et al., 2008; Choudhury, 1999). Central to these equations is a catchment-specific parameter (commonly denoted as ω or n), which functions as an integrated metric of landscape characteristics, encapsulating the effects of vegetation dynamics, soil properties, and topography on the water balance (Zhang et al., 2001; Yang et al., 2008). However, under the intensifying influence of the Anthropocene, the driving mechanisms of this parameter have become increasingly intricate. ω is no longer a static attribute defined solely by natural geography; instead, it evolves dynamically in response to multiple interacting forces—ranging from ecological restoration (e.g., vegetation greening) to intensive landscape reengineering (e.g., terracing) and socioeconomic water withdrawal (Liang et al., 2015; Feng et al., 2016). These anthropogenic perturbations interact with climatic fluctuations, creating highly nonlinear responses and threshold effects that traditional linear statistical methods struggle to capture (Shen, 2018; Shen et al., 2017). Therefore, accurately decoding the multidimensional drivers of ω is the key to revealing the changing hydrological mechanisms in these transition zones.

Furthermore, the spatial heterogeneity of catchment functioning within similar climatic zones remains insufficiently understood. Traditional attribution studies often adopt a “top-down” perspective, implicitly assuming that catchments situated within the same macroclimatic belt share homogeneous hydrological behaviors and driving mechanisms (Wagener et al., 2007; Gupta et al., 2014). However, this assumption of spatial stationarity often masks significant intrazonal

https://doi.org/10.5194/egusphere-2026-969
Preprint. Discussion started: 26 February 2026

heterogeneity (Sawicz et al., 2011; Oudin et al., 2008). In reality, hydrological response is a result of the coevolution of climate and catchment characteristics. Local landscape attributes—such as specific geomorphic features (e.g., slope gradient and roughness) and distinct modes of human intervention (e.g., terracing vs. urbanization)—can significantly alter flow pathways, engendering hydrological regimes that deviate from the regional average (Troch et al., 2015; Li et al., 2021; Beven, 2000). Overlooking this "uniqueness of place" constrains the development of targeted management strategies, as "one-size-fits-all" models may fail to capture the dominant drivers in catchments undergoing rapid local transformation (Sivapalan, 2003; Blöschl, 2013). Specifically, within the Budyko framework, this heterogeneity manifests as the complex spatial variability in the parameter ω. The mapping from multidimensional local attributes to ω involves intricate nonlinear interactions and threshold effects, which remain effectively a "black box" to traditional linear attribution models (Zhang et al., 2004; Shen et al., 2017).

To address these methodological challenges, data-driven machine learning (ML) offers a powerful diagnostic approach; however, the selection of an optimal modeling structure remains critical. Hydrological responses in transition zones involve high-dimensional interactions that may be captured differently by algorithms with distinct inductive biases (Shen, 2018; Reichstein et al., 2019). For instance, tree-based ensemble methods, such as random forest (RF) and extreme gradient boosting (XGBoost), handle abrupt thresholds and nonlinearities well, connectionist models (e.g., artificial neural networks, ANN) are often superior in approximating smooth continuous functions, and kernel-based methods (e.g., support vector machines, SVM) offer robustness in high-dimensional feature spaces (Shortridge et al., 2016; Ding et al., 2025). Consequently, relying on a single algorithm without rigorous comparison may yield results that are artifacts of the model structure rather than true hydrological signals. A systematic benchmarking strategy across these diverse algorithms is therefore essential for quantifying structural uncertainty and identifying the most robust architecture for this specific region (Papacharalampous et al., 2019; Sit et al., 2020). Furthermore, to overcome the "black-box" nature of the optimal model, integrating it with SHAP (Shapley Additive exPlanations) provides a unified measure to quantitatively disentangle marginal contributions and visualize nonmonotonic response curves, ensuring the physical interpretability of the results (Murdoch et al., 2019; Lundberg and Lee, 2017).

In this study, using the Yellow River Basin as a representative microcosm of semiarid to semihumid transition zones, we propose a machine learning-driven diagnostic framework to clarify the spatially divergent drivers of hydrological function. Specifically, we proposed a diagnostic framework that systematically benchmarked four machine learning algorithms—XGBoost, RF, ANN, and SVM—to identify the optimal tool for capturing the nonlinear dynamics of ω. By integrating the best-performing model with SHAP analysis and objective functional zoning, this study aims to (1) objectively classify the catchments into distinct hydrological functional zones on the basis of multidimensional characteristics; (2) quantify the shifting dominance of climatic, anthropogenic, and landscape drivers across these zones; and (3) reveal the critical nonlinear thresholds and interaction mechanisms that define these divergent regimes. Ultimately, this work seeks to provide a mechanism-based scientific basis for spatially differentiated water resource management.

https://doi.org/10.5194/egusphere-2026-969
Preprint. Discussion started: 26 February 2026

2 Materials and Methods

2.1 Study Area

We selected 12 representative catchments in the Yellow River Basin, China, traversing a pronounced hydroclimatic gradient from semi-arid to semi-humid zones (Fig. 1). These catchments display a clear spatial divergence in underlying surface characteristics. The semi-arid regions are primarily dominated by grasslands, whereas the transitional semi-arid/semi-humid regions feature a mosaic of forests and grasslands. Conversely, the semi-humid regions are heavily modified by anthropogenic activities and characterized by extensive croplands and impervious surfaces. The hydrological functioning of these catchments is complex and driven by the interplay of static landscape features (e.g., topography and soil) and dynamic environmental changes (Peng et al., 2025). Specifically, climate warming, land use/cover change, and anthropogenic water consumption act as concurrent drivers that directly or indirectly reshape runoff generation processes across the basin.

https://doi.org/10.5194/egusphere-2026-969
Preprint. Discussion started: 26 February 2026

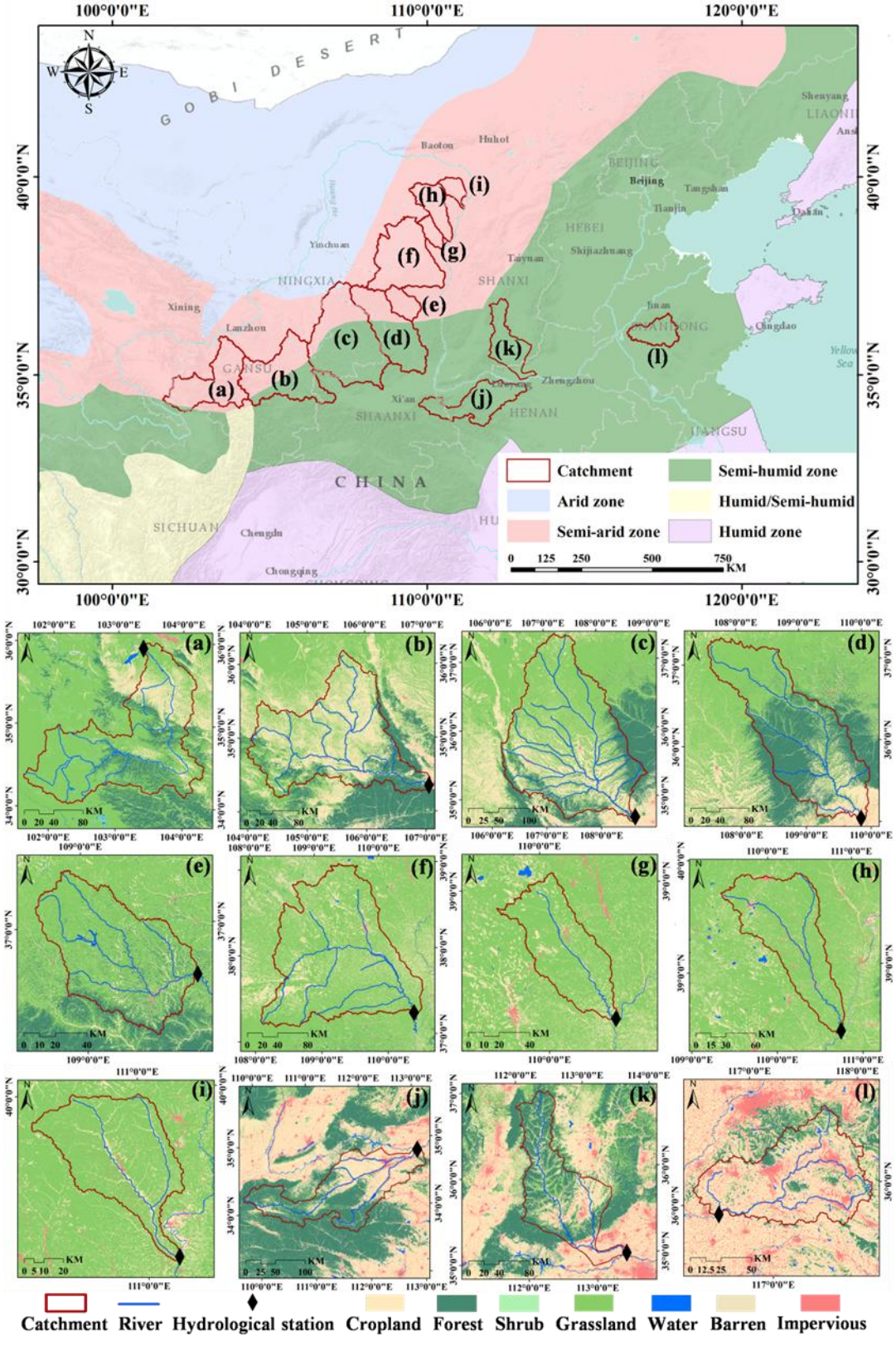

110

https://doi.org/10.5194/egusphere-2026-969
Preprint. Discussion started: 26 February 2026

Figure 1: Study area and catchment characteristics. (Top) Locations of the 12 catchments overlaid on different climatic zones. (Bottom) Detailed views (a–l) showing the land use composition (see legend), river systems, and outlets for each catchment.

2.2 Overview of the Analytical Framework

To differentiate the spatially divergent drivers of the Budyko-type equation parameter ω, this study proposes a machine learning-driven diagnostic framework consisting of three integrated steps (Fig. 2). (1) Objective Zoning: Identifying hydrological functional zones on the basis of the long-term catchment characteristics of the 12 catchments spanning different climatic zones, principal component analysis (PCA) coupled with hierarchical clustering was used. (2) Cluster-based Modeling: Benchmarking four machine learning algorithms (XGBoost, RF, ANN, and SVM) to simulate ω within each identified zone, incorporating 13 feature variables categorized into climatic, anthropogenic, and landscape drivers, to identify the optimal model for attribution analysis. (3) Mechanism Diagnosis: Interpreting the driving mechanisms using SHAP analysis based on the optimal model and explicitly clarifying how climatic, anthropogenic, and landscape factors differentially influence ω variations across distinct functional zones.

https://doi.org/10.5194/egusphere-2026-969
Preprint. Discussion started: 26 February 2026

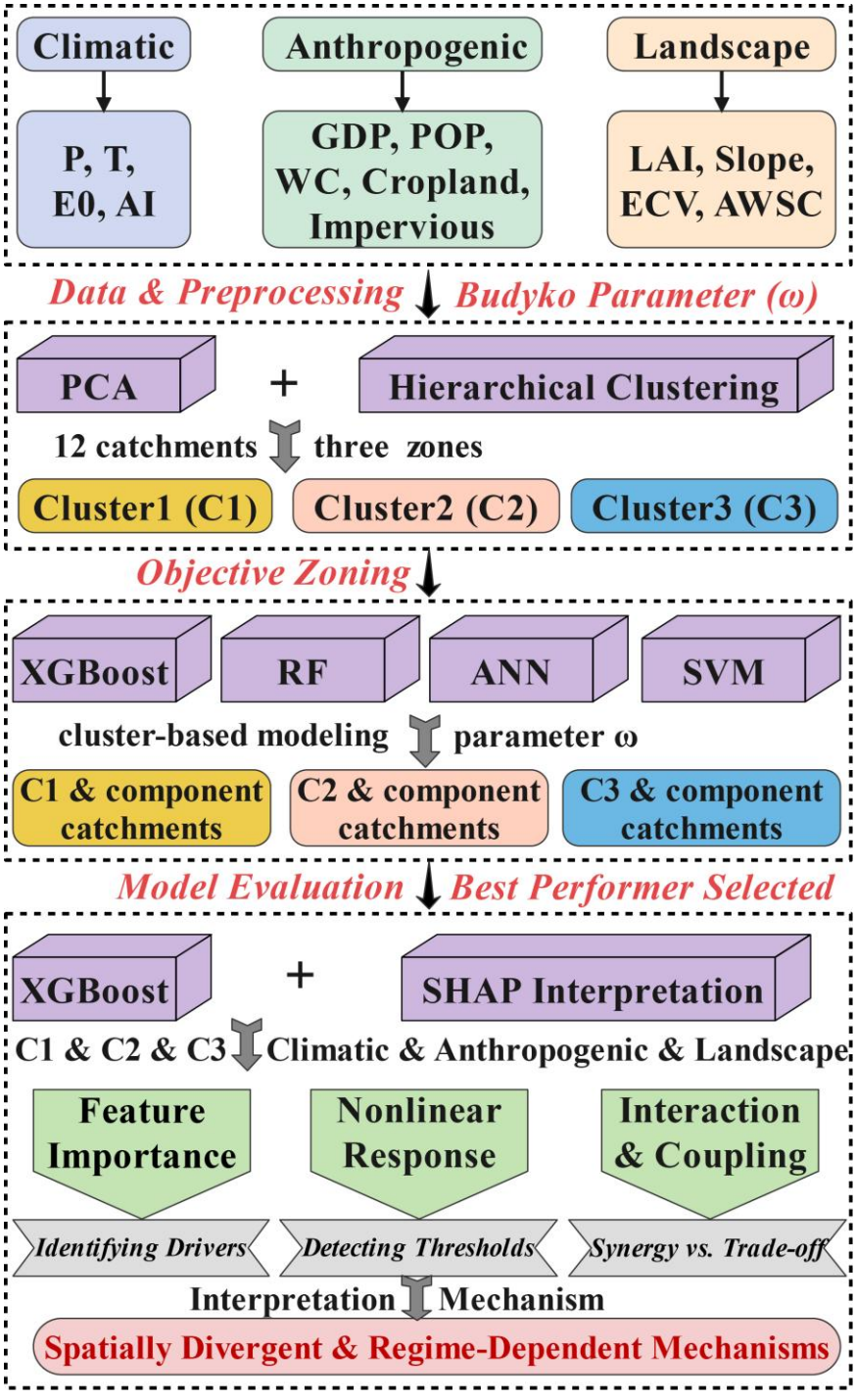

Figure 2: Methodological framework of the study. The framework consists of four integrated steps. (1) Data and Preprocessing: Construction of a multisource dataset comprising climatic, anthropogenic, and landscape drivers. (2) Objective Zoning: Identification of three hydrological functional zones (C1, C2, and C3) using PCA coupled with hierarchical clustering. (3) Model Evaluation: Selection of XGBoost as the optimal model through a robust performance comparison with RF, ANN, and SVM. (4)

https://doi.org/10.5194/egusphere-2026-969
Preprint. Discussion started: 26 February 2026

Interpretation and Mechanism: Determination of the dominant drivers, nonlinear responses, and interaction effects using SHAP analysis to explain the spatially divergent mechanisms.

2.3 Calculation of the Time-Varying Budyko Parameter (ω)

To quantify the integrated impact of catchment characteristics on the water-energy balance, we employed Fu's equation (Fu, 1981), a widely recognized analytical solution to the Budyko hypothesis. The relationship is expressed as follows:

$$\frac{E}{P} = 1 + \frac{E_0}{P} - \left[1 + \left(\frac{E_0}{P}\right)^{\omega}\right]^{1/\omega} \quad (1)$$

Combined with the long-term catchment water balance equation ($E = P - R$, assuming negligible water storage change over multiyear periods), the runoff (R) can be estimated as follows:

$$R = P\left(\left[1 + \left(\frac{E_0}{P}\right)^{\omega}\right]^{1/\omega} - \frac{E_0}{P}\right) \quad (2)$$

where P, R, E, and E_0 denote precipitation, runoff, actual evapotranspiration, and potential evapotranspiration, respectively. The observed annual runoff data were obtained from the Yellow River Conservancy Commission of the Ministry of Water Resources (http://www.yrcc.gov.cn/). The parameter ω represents the catchment characteristics (e.g., vegetation, soil properties, and topography) that modify the partitioning of precipitation into evaporation and runoff. A higher ω indicates a higher evaporative capacity (or lower runoff coefficient) under the same climatic conditions.

To capture the temporal evolution of hydrological functioning, we calculated the time-varying ω using an 11-year moving window approach for each catchment during the study period. This approach was adopted to minimize the impacts of interannual terrestrial water storage changes, ensuring the validity of the steady-state assumption required by the Budyko framework while preserving long-term trends. Specifically, for each window, the value of ω was numerically inverted by matching the observed annual runoff with the theoretical runoff derived from Fu's equation.

2.4 Variable Construction and Preprocessing

To investigate the driving factors underlying the spatiotemporal variations in ω, we constructed a comprehensive dataset of 13 potential drivers categorized into three groups: climate, anthropogenic, and landscape drivers (Table 1). Climatic drivers include precipitation (P), temperature (T), potential evapotranspiration (E_0), and the aridity index (AI), which represent the atmospheric water and energy supply and demand, respectively. Anthropogenic drivers include population density (POP), GDP density (GDP), water consumption (WC), and land use proportions ($Cropland$ and $Impervious$), which represent external human disturbances. Notably, to eliminate the scale effect of catchment size, all volume-based socioeconomic variables (e.g., GDP and WC) were normalized by catchment area to quantify the intensity of human activity per unit area. Landscape drivers characterize the biophysical attributes of the catchment surface; they encompass static topographic and soil features ($Slope$, ECV, and $AWSC$) as well as dynamic biophysical properties (LAI), representing the regulatory capacity

https://doi.org/10.5194/egusphere-2026-969
Preprint. Discussion started: 26 February 2026

of the underlying surface. Specifically, $AWSC$ was calculated by integrating soil water retention properties with the effective rooting depth.

Table 1. Summary of climatic, anthropogenic, and landscape variables used in this study.

Category	Variable	Abbr.	Unit	Description
Climatic	Precipitation	***P***	mm	Annual accumulated precipitation
	Temperature	***T***	°C	Mean annual air temperature
	Potential Evapotranspiration	***E0***	mm	Annual accumulated potential evapotranspiration
	Aridity Index	***AI***	—	*P*/*E*0
Anthropogenic	Population Density	***POP***	person/km²	Annual population density
	Gross Domestic Product	***GDP***	USD/km²	Annual GDP per unit area
	Water Consumption	***WC***	mm	Annual total water withdrawal
	Cropland Proportion	***Cropland***	%	Annual areal proportion of cropland
	Impervious Surface	***Impervious***	%	Annual areal proportion of impervious surfaces
Landscape	Leaf Area Index	***LAI***	m²/m²	Annual mean LAI
	Slope	***Slope***	degree	Mean topographic slope derived from DEM
	Elevation Coeff. of Variation	***ECV***	—	Coefficient of variation of elevation (Roughness)
	Available Water Storage Capacity	***AWSC***	mm	Effective root-zone water storage capacity

2.5 Objective Functional Zoning via PCA and Hierarchical Clustering

To address the spatial heterogeneity of hydrological functioning, we applied a two-step objective zoning approach based on the long-term mean characteristics of the 12 catchments. First, PCA was performed to reduce dimensionality and eliminate multicollinearity among the 13 drivers. The original feature matrix X $(n \times p)$ was standardized to Z, and the principal components (PCs) were derived via linear transformation:

$$Y = ZW \tag{3}$$

where Y is the matrix of principal component scores and W is the matrix of eigenvectors derived from the covariance matrix of Z.

Hierarchical clustering was subsequently applied to the significant PCs using Ward's linkage method with Euclidean distance as the similarity metric. To quantitatively determine the optimal number of clusters (k), we employed the silhouette coefficient method. For a given data point i, the silhouette value $s(i)$ is defined as follows:

https://doi.org/10.5194/egusphere-2026-969
Preprint. Discussion started: 26 February 2026

$$s(i) = \frac{b(i)-a(i)}{max\{a(i),b(i)\}} \quad (4)$$

where $a(i)$ is the average distance between i and all other points in the same cluster and $b(i)$ is the minimum average distance from i to points in a different cluster. The optimal k was identified as 3, corresponding to the maximum average silhouette width, ensuring the statistical robustness of the classification.

2.6 Cluster-based Machine Learning Modeling

To investigate the driving mechanisms of the catchment characteristic parameter (ω), we developed machine learning regression models using ω as the target variable and the 13 identified climatic, anthropogenic, and landscape factors as predictors. We adopted a "cluster-based modeling" strategy, constructing independent models for each functional zone. To identify the optimal algorithm, we benchmarked four machine learning models: XGBoost, RF, ANN, and SVM. For model training and validation, we employed a stratified random sampling method based on catchment identity. Specifically, 70% of the samples from each individual catchment were randomly selected to form the training set, while the remaining 30% constituted the independent test set. The hyperparameters were optimized using 5-fold cross-validation on the training set to prevent overfitting.

Notably, a hierarchical evaluation strategy was employed to select the optimal model. First, the overall performance was assessed on the aggregated test set of each cluster using the coefficient of determination (R^2) and root mean square error ($RMSE$). Second, to ensure the robustness of the model against intercatchment heterogeneity, cluster-trained models were applied to simulate ω for each individual catchment within the corresponding cluster. The optimal model was ultimately selected on the basis of a comprehensive assessment of both cluster-level accuracy and catchment-level stability.

2.7 Interpretable Analysis using SHAP

To open the “black box” of the machine learning models and quantify the specific contributions of driving factors, we employed SHAP based on cooperative game theory (Lundberg and Lee, 2017). The SHAP value (ϕ) represents the marginal contribution of a specific feature to the deviation of the model's prediction from the mean prediction. Mathematically, the prediction for a specific sample i ($\hat{y}_i$) is expressed as the sum of the baseline value (ϕ_0) and the SHAP values of all M features:

$$\hat{y}_i = \phi_0 + \sum_{j=1}^{M} \phi_{i,j} \quad (5)$$

where $\phi_{i,j}$ denotes the SHAP value of feature j for sample i. We derived the global feature importance by calculating the mean absolute SHAP value to rank the dominant drivers within each functional zone. Furthermore, SHAP dependence plots were generated to visualize the marginal response curves of ω to key drivers, thereby revealing the nonlinear relationships and identifying critical threshold effects.

https://doi.org/10.5194/egusphere-2026-969
Preprint. Discussion started: 26 February 2026

Beyond individual features, we further quantified the collective effects of the three driver categories—climatic, anthropogenic, and landscape—to analyze their systemic interactions. The groupwise aggregated SHAP value (Φ) for a specific category G was calculated by summing the SHAP values of all the features belonging to that category:

$$\Phi_{i,G} = \sum_{j \in G} \phi_{i,j} \quad (6)$$

By analyzing the sign and magnitude of Φ, we determined the net directional impact (positive or negative) of each driver category on ω. Moreover, by comparing the signs of Φ among different categories for the same sample, we identified the interaction patterns of driving forces, distinguishing between synergy (where drivers act in the same direction) and trade-offs (where drivers counteract each other) across different hydrological regimes.

3 Results

3.1 Spatiotemporal Evolution of Catchment Characteristics (ω)

The spatiotemporal evolution and statistical distribution of the catchment characteristic parameter (ω) across the 12 catchments are shown in Fig. 3. Temporally, a predominant increasing trend was observed in most catchments from 1985 to 2015. As shown in the heatmap (Fig. 3, top), the color intensity generally shifted from light to dark over the three decades. For instance, in catchment e, the ω value increased notably from 2.96 in 1985 to 3.36 in 2015, whereas that in catchment g increased from 1.74 to 2.10. This widespread upward trend suggests a consistent shift in the underlying surface conditions across the catchment, enhancing the capacity for evapotranspiration and water retention over time.

Spatially, ω exhibited significant heterogeneity across the study area. The multiyear average values ranged widely from 1.93 to 3.42 (Fig. 3, bottom). Catchments g and a displayed the lowest multiyear averages of 1.93 and 2.01, respectively, indicating a runoff-dominated regime. In contrast, catchments d and c maintained the highest average values of 3.42 and 3.33, respectively, reflecting a strong evaporative capacity. The violin and box plots further reveal distinct patterns of temporal variability independent of the mean magnitude. Catchments I and h exhibited elongated probability density curves with wide interquartile ranges, highlighting substantial interannual fluctuations and potential regime shifts. Conversely, other catchments displayed highly compact distributions, indicating relatively stable hydrological functioning, regardless of whether their baseline ω is low (e.g., g and a) or high (e.g., k).

In summary, the significant spatiotemporal heterogeneity and distinct distributional patterns of ω suggest that the underlying driving mechanisms of catchment functioning are likely nonuniform across different catchments. This complexity highlights the limitations of a unified explanation and necessitates an objective functional zoning approach to clarify the different roles of climatic, anthropogenic, and landscape factors in subsequent sections.

https://doi.org/10.5194/egusphere-2026-969
Preprint. Discussion started: 26 February 2026

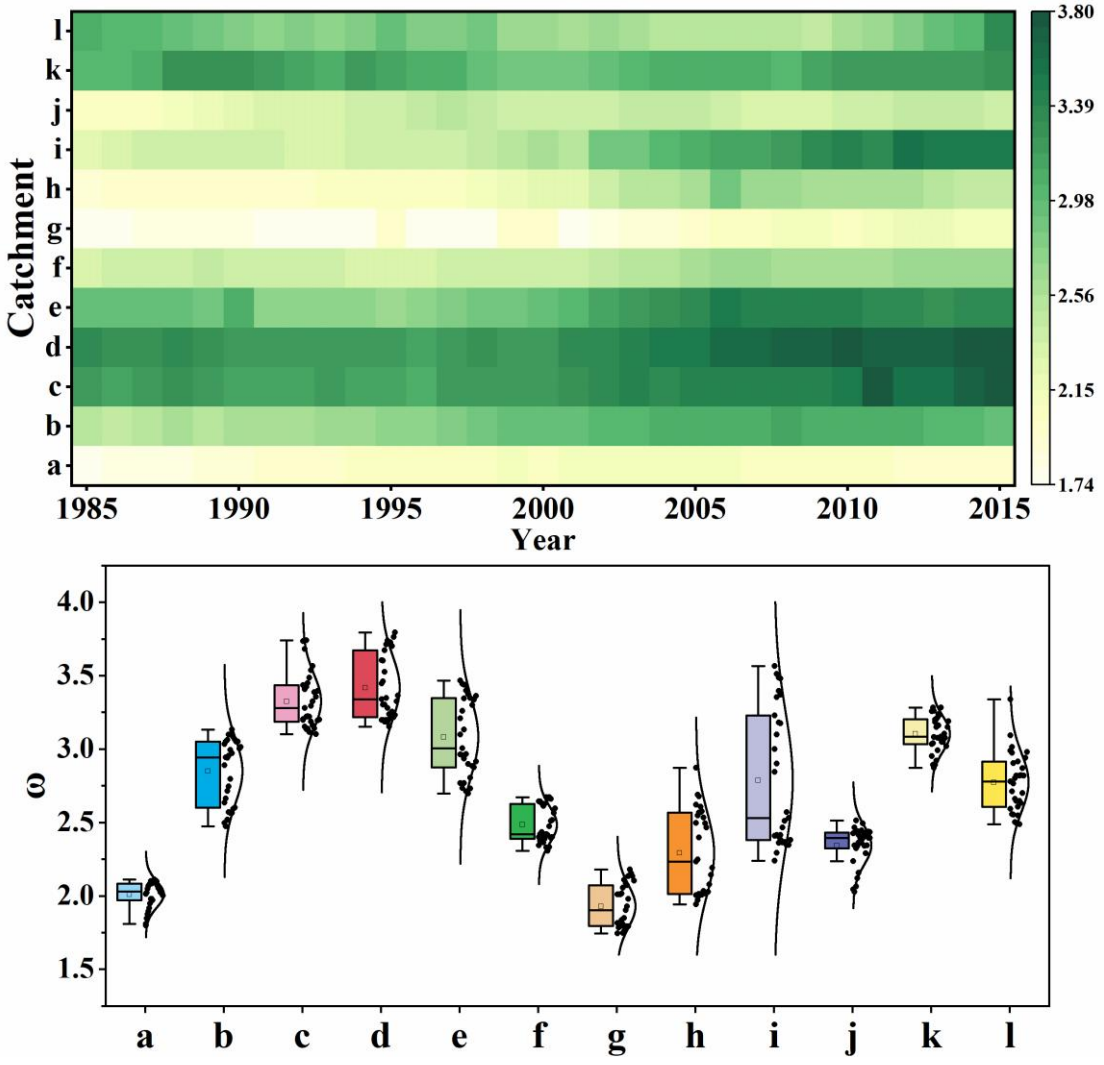

Figure 3: Spatiotemporal evolution and statistical distribution of the catchment characteristic parameter (ω) across the 12 study catchments. (Top) Heatmap showing the temporal variation in ω. The x-axis represents the central year (1985–2015) of the 11-year moving window derived from the 1980–2020 data series. (Bottom) Statistical distribution of ω visualized using violin plots combined with box plots. The box plots indicate the median (centerline), interquartile range (box), and whiskers; the violin plots illustrate the probability density distribution; and the scattered dots represent individual annual values.

3.2 Statistical Identification and Characterization of Functional Zones

The application of PCA and hierarchical clustering objectively categorized the 12 catchments into three distinct groups based on their long-term hydroclimatic, anthropogenic, and landscape characteristics (Fig. 4). Dimensionality reduction analysis revealed that the first two principal components (PCs) explained 85.1% of the total variance in the dataset. As shown in Fig. 4a, PC1 (61.1%) was primarily loaded by hydroclimatic abundance (e.g., P and $AWSC$) and anthropogenic intensity (e.g.,

https://doi.org/10.5194/egusphere-2026-969
Preprint. Discussion started: 26 February 2026

GDP and POP), whereas PC2 (24.0%) was largely defined by topographic features ($Slope$). Hierarchical clustering (Fig. 4b) and PCA biplots (Fig. 4c) consistently revealed three robust clusters occupying distinct niches in the feature space: Cluster 1 (C1) in the lower-right quadrant, Cluster 2 (C2) in the upper-left quadrant, and Cluster 3 (C3) in the upper-right quadrant. The heatmap (Fig. 4d) further provides a quantitative characterization of these clusters, revealing substantial divergences in their underlying properties. C1, comprising five catchments (a–e), is uniquely distinguished by its complex topography, with the highest mean slope (17.6 degrees) among all the groups. Climatically, this group represents a relatively cool environment with the lowest mean annual temperature of 7.89 °C, while its anthropogenic footprint remains moderate compared with that of other regions. In stark contrast, C2 (catchments j–l) is characterized by the most favorable hydrothermal conditions and the highest intensity of human activity. This group recorded the highest mean annual precipitation (603 mm), temperature (12.3 °C), and vegetation cover (LAI = 1.14). Notably, it also serves as the socioeconomic center of the study area, with a GDP density of 2.8×10^6 USD/km² and a population density of 1.1×10^7 person/km²—values that are orders of magnitude greater than those in the other two clusters, indicating that the landscape is heavily shaped by both natural resources and human development. Conversely, C3 (catchments f–i) represents the most water-limited environment within the basin. This group exhibits the highest atmospheric water demand, with a potential evapotranspiration (E_0) of 1122 mm, but received the lowest precipitation (375 mm), resulting in an extremely low aridity index (AI) of 0.33. Consequently, the landscape in Cluster 3 is characterized by poor water retention capacity ($AWSC$ = 44.4 mm) and sparse vegetation (LAI = 0.27), reflecting a fragile ecosystem under severe water stress. These distinct characteristic profiles—topographically complex (C1), resource-rich and developed (C2), and water-scarce (C3)—provide the physical basis for investigating their divergent hydrological responses in the subsequent analysis.

https://doi.org/10.5194/egusphere-2026-969
Preprint. Discussion started: 26 February 2026

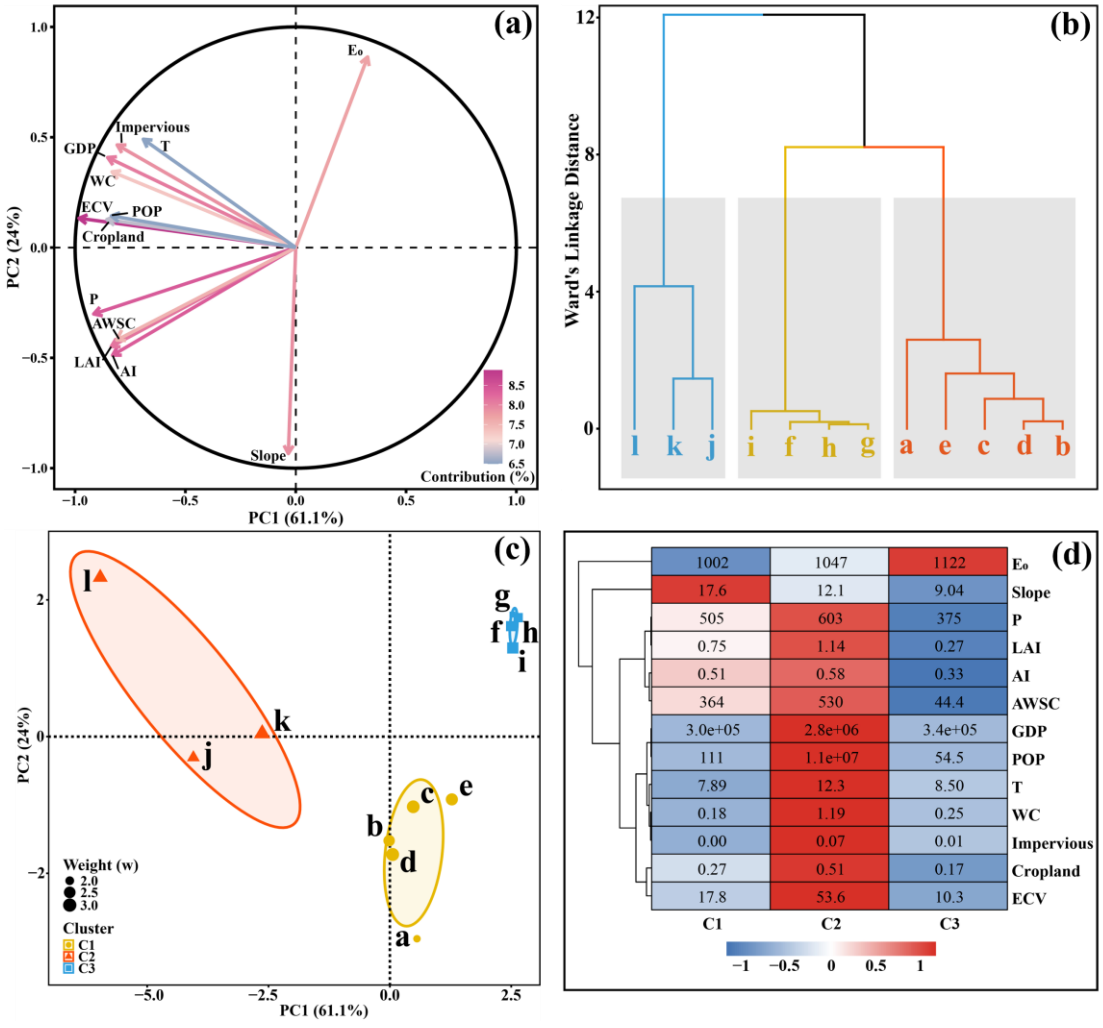

Figure 4: Statistical identification and characterization of hydrological functional zones. (a) PCA loading plot showing the relationships and contributions of climatic, anthropogenic, and landscape drivers to the first two principal components. (b) Dendrogram from hierarchical clustering (Ward's method), identifying three distinct clusters. (c) PCA biplot visualizing the distribution of the 12 catchments in the feature space, grouped by the identified clusters. (d) Heatmap of the mean feature profiles for each cluster. The colors represent the normalized z scores, with the actual mean values displayed in the cells.

3.3 Performance Comparison and Selection of Machine Learning Models

To identify the most robust tool for attribution analysis, we systematically benchmarked four machine learning algorithms (XGBoost, RF, ANN, and SVM) based on a comprehensive assessment of both overall accuracy (Table 2) and intercatchment stability (Fig. 5). In terms of overall accuracy, XGBoost demonstrated the best balance across the functional zones. As shown in Table 2, in C2, owing to the high nonlinearity of hydrological processes caused by the intricate coupling of intensive agriculture and vegetation dynamics, XGBoost achieved both the highest R^2(0.967) and lowest RMSE (0.061), significantly outperforming ANN ($R^2 = 0.784$) and SVM ($R^2 = 0.797$). In C3, XGBoost demonstrated superior

https://doi.org/10.5194/egusphere-2026-969
Preprint. Discussion started: 26 February 2026

performance across all the metrics, attaining both the highest R^2 (0.983) and the lowest RMSE (0.056), indicating its robust ability to explain the variability of ω. Similarly, in C1, ANN showed a slightly higher R^2 (0.995 vs. 0.991), likely because the continuous climatic drivers in this zone align well with the smooth function approximation capabilities of neural networks; however, XGBoost still maintained the lowest prediction error ($RMSE = 0.053$).

Table 2. Performance comparison of the four machine learning models for predicting the catchment characteristic parameter (ω) across the three zones.

Model	C1		C2		C3	
	R^2	RMSE	R^2	RMSE	R^2	RMSE
XGBoost	0.991	***0.053***	***0.967***	***0.061***	***0.983***	***0.056***
RF	0.988	0.059	0.916	0.099	0.955	0.082
ANN	***0.995***	0.056	0.784	0.160	0.963	0.067
SVM	0.980	0.077	0.797	0.155	0.956	0.080

Crucially, the distributional characteristics of model performance, assessed by both R^2 and the RMSE, highlighted the superior stability of XGBoost against intercatchment heterogeneity (Fig. 5). In the C1 and C3 regimes, XGBoost demonstrated exceptional robustness. As shown in the violin plots, XGBoost consistently maintained compact distributions with high accuracy. Notably, in C3, XGBoost successfully avoided extreme performance failures, maintaining a minimum R^2 of 0.701, whereas the values of SVM and RF significantly decreased, to 0.404 and 0.570, respectively. The advantage of XGBoost became even more evident when the RMSE in C2 was examined. While RF and SVM yielded higher median correlations R^2, they experienced severe instability in prediction accuracy. Specifically, the RMSEs for ANN and SVM in C2 spiked to 0.255 and 0.249, respectively, for certain catchments, and RF also recorded a high error of 0.122. In sharp contrast, XGBoost constrained the RMSE of all the catchments within a remarkably low range (< 0.064). This finding indicates that while other models might fit the trend well in some cases, they are prone to producing large absolute errors in complex scenarios. Conversely, XGBoost minimizes extreme deviations. Therefore, considering its ability to prevent large errors (lowest maximum RMSE) and avoid model collapse (highest minimum R^2), XGBoost was selected as the most reliable tool for the subsequent attribution analysis.

Thus, considering the trade-off between metrics and regimes, XGBoost was selected as the optimal regressor. The validation scatter plots (Fig. 6) further confirm this choice, showing that the ω values predicted by XGBoost are tightly clustered around the 1:1 identity line for all three zones, with R^2 exceeding 0.967 and the RMSE remaining below 0.061. This high accuracy ensures a solid physical basis for the subsequent SHAP-based mechanism analysis.

https://doi.org/10.5194/egusphere-2026-969
Preprint. Discussion started: 26 February 2026

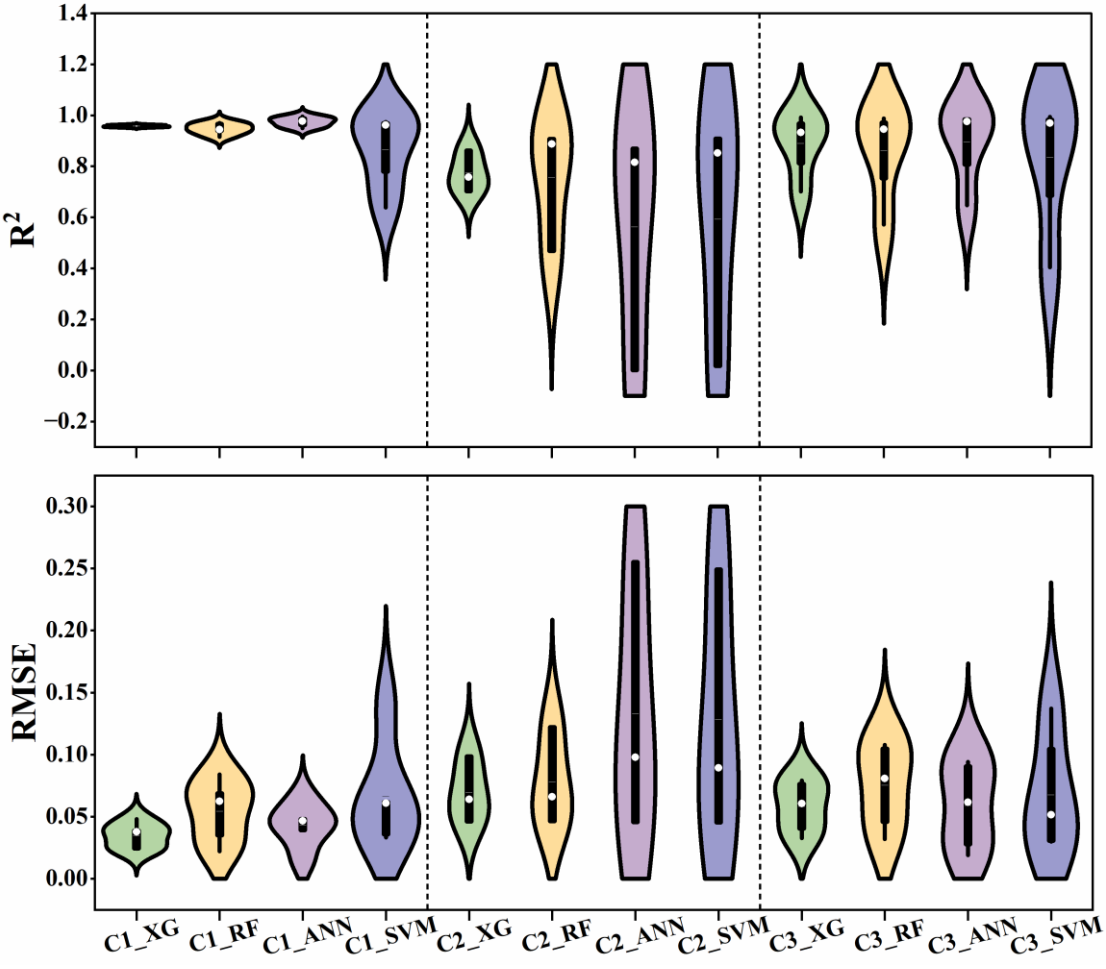

Figure 5: Comparison of model performance distributions across the three zones. Violin plots display the distributions of (top) R2 and (bottom) RMSE for XGBoost (XG), RF, ANN, and SVM within each cluster. The white dots represent the median, the thick black bars represent the interquartile range, and the shape represents the probability density of the performance metrics across individual catchments.

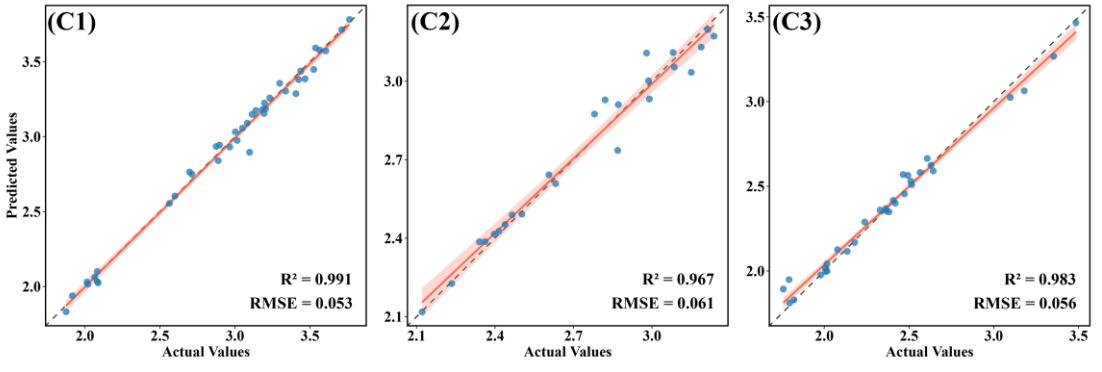

Figure 6: Evaluation of the performance of the XGBoost model in predicting ω across the three zones (validation set).

https://doi.org/10.5194/egusphere-2026-969
Preprint. Discussion started: 26 February 2026

3.4 Dominant Drivers and Directional Impacts

The SHAP-based interpretation reveals distinct driving mechanisms and directional impacts of key factors across the three zones (Fig. 7). In C1, T, AI, and P are identified as the top three dominant drivers, collectively accounting for 47.92% of the total feature importance. The SHAP summary plot indicates distinct directional impacts: high values of T and P (purple dots) correspond to positive SHAP values, indicating a positive contribution to ω. In contrast, high AI values result in a negative contribution, suggesting that while precipitation increases ω, a higher overall wetness index (relative to evaporation demand) tends to decrease ω in this region. This contrast highlights the delicate balance between water supply and energy limitation within this transitional zone. In C2, LAI, POP, and AI rank as the top three drivers, with a combined importance of 49.41%. Notably, the summary plot reveals a distinct negative driving pattern: high values of these three factors are predominantly distributed in the negative region (SHAP < 0), implying that they all tend to decrease ω. Similarly, T (ranked 4th) also has a negative effect at high values. This finding contrasts sharply with the pattern observed in C1, highlighting that the same factor can have different effects across different functional zones. In C3, GDP, $Slope$, and $Impervious$ occupy the top three positions, accounting for 66.53% of the importance and playing a dominant role. The plot highlights a mechanism characterized by positive enhancement: high values of these factors are concentrated in the positive region and significantly increase ω. However, WC (ranked 4th) shows the opposite trend, where high water withdrawal acts as a negative driving force, lowering the ω value.

https://doi.org/10.5194/egusphere-2026-969
Preprint. Discussion started: 26 February 2026

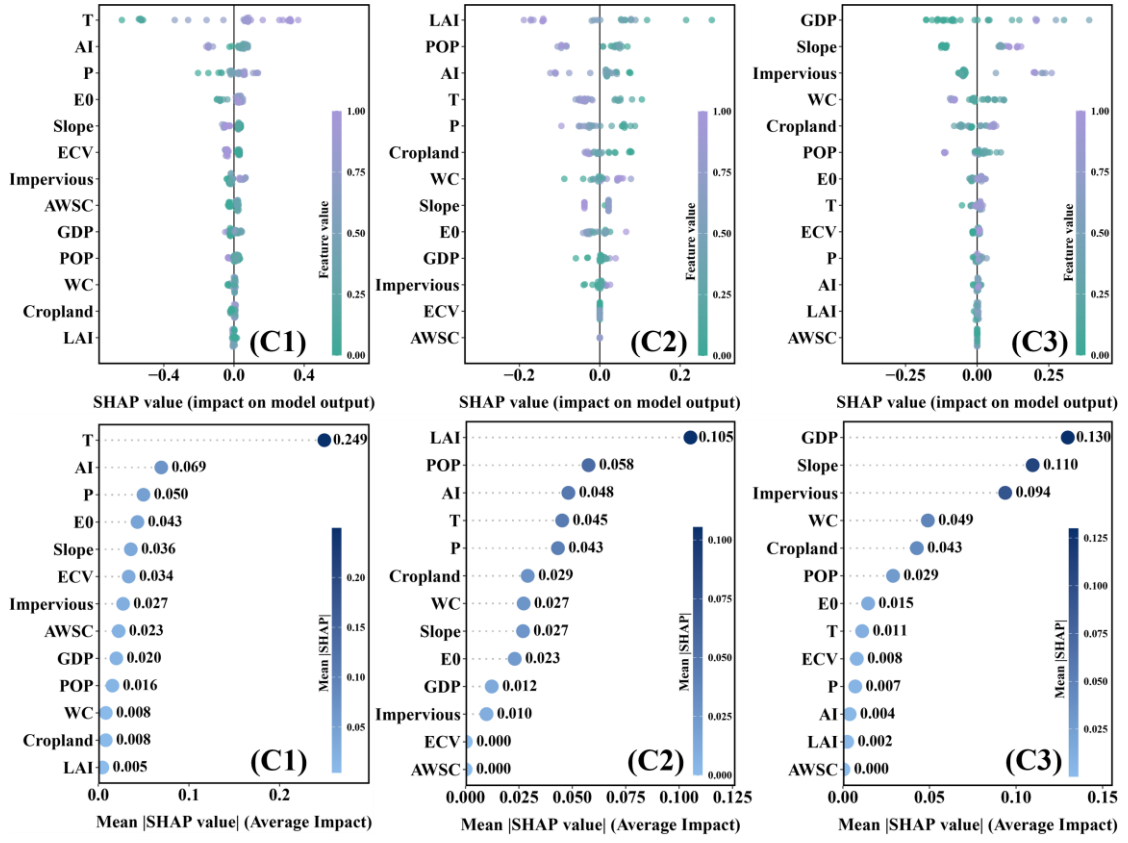

Figure 7: Directional impacts and global feature importance rankings of drivers on ω across the three zones. (Top) SHAP summary plots illustrating the distribution and directional contribution of each feature. Each dot represents a sample; the color indicates the feature value; and the x-axis indicates the SHAP value (impact on ω). (Bottom) Bar charts displaying the global feature importance, ranked by the mean absolute SHAP values.

3.5 Nonlinear Responses and Systemic Interactions

SHAP dependence plots (Fig. 8) further elucidate the complex nonlinear relationships between ω and the top three driving factors, identifying critical tipping points where SHAP values shift between positive and negative. In C1, the influence of T on ω exhibits a classic "S-shaped" curve. SHAP values increase with T and become positive only when T exceeds 8.17 °C, indicating a positive contribution to ω once the energy constraint is lifted. AI displays a nonmonotonic "hump-shaped" response. It promotes ω within a moderate range but becomes a negative driver when AI drops below 0.42 (too dry) or exceeds 0.55 (too wet). This highlights a narrow optimal window for high ω values. For P, a general increasing trend is observed, where the SHAP values transition from negative to positive as the annual precipitation exceeds 497 mm. In C2, the SHAP values generally show a fluctuating downward trend as the three factors increase. LAI exerts a positive effect when it is less than 1.16 but decreases sharply below zero once it exceeds this threshold. This result suggests that excessively dense vegetation tends to decrease ω, likely because of soil saturation during the rainy season or agricultural drainage practices. Similarly, POP shows a threshold effect at $1{,}172 \times 10^4$; beyond this point, it has a negative influence on ω, possibly

https://doi.org/10.5194/egusphere-2026-969
Preprint. Discussion started: 26 February 2026

because the intensification of urbanization overrides consumption effects. *AI* in this region also displays a clear threshold at 0.62, above which wetter conditions significantly decrease ω, reflecting a shift from water-limited to energy-limited conditions. In C3, the SHAP values generally increase as the three factors increase. The response to GDP follows a distinct 'inverted-U' curve, showing a negative contribution before the threshold of 25.8×10^4. With respect to $Slope$, a clear physical threshold is identified at 8.8°. Below this gradient, the contribution is negative; however, above 8.8°, the contribution becomes strongly positive. For $Impervious$, the threshold is 0.016; in this arid environment, higher $Impervious$ coverage consistently pushes ω upward, possibly because of the urban heat island effect.

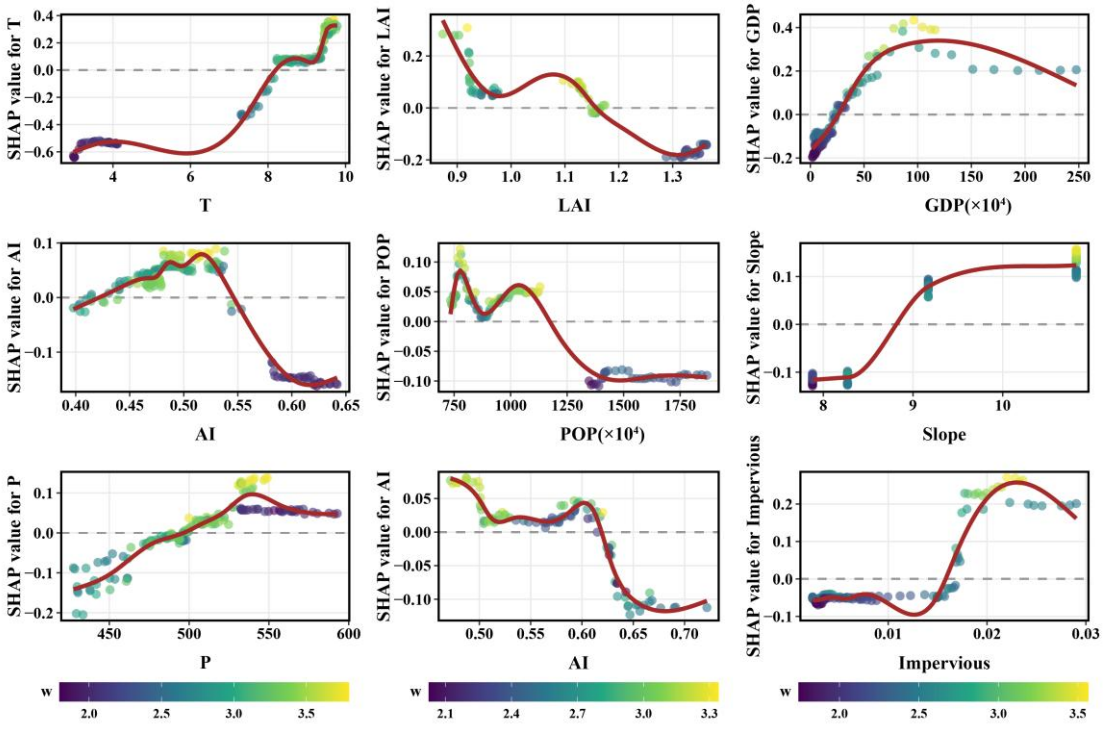

Figure 8: SHAP dependence plots illustrating the nonlinear response mechanisms of ω to the top-ranked drivers across the three zones. The panels display the marginal effect of the top three most important features on the model output (ω). The x-axis represents the actual value of the feature, and the y-axis represents the SHAP value (impact on ω). The color of the dots indicates the magnitude of ω. The red lines are smooth curves fitted to visualize the overall trends.

Beyond individual factors, the aggregated SHAP analysis (Fig. 9) reveals the collective influence of climate, anthropogenic, and landscape drivers on ω from a systemic perspective. First, the net directional impacts vary significantly across different functional zones (Fig. 9a). In C1, the climate and landscape drivers exhibit a dominant positive contribution, with 65.16% and 59.35% of the samples showing positive aggregated SHAP values, respectively. In contrast, anthropogenic drivers primarily make a negative contribution, accounting for 62.58% of the sample. Similarly, in C2, anthropogenic drivers also display a dominant negative impact (63.71% negative), indicating that intensive anthropogenic activities generally tend to decrease ω. The proportions of positive contributions for the climate and landscape drivers are 55.65% and 50.00%,

https://doi.org/10.5194/egusphere-2026-969
Preprint. Discussion started: 26 February 2026

respectively. In C3, landscape drivers have a strong positive effect (66.67% positive), whereas climate drivers have a negative effect (54.84% negative). With respect to anthropogenic drivers, the proportion of negative contributions is 44.09%. Second, the interaction analysis reveals distinct patterns of synergy and trade-offs (Fig. 9b). In C1, the interaction between the climate and landscape drivers ($C \cap L$) exhibit the strongest positive synergy (accounting for 50.32%). Similarly, the interaction between climate and anthropogenic drivers ($C \cap A$) is also predominantly positive (35.48%). However, unlike the other pairs, the interaction between anthropogenic and landscape drivers ($A \cap L$) is dominated by divergent trade-offs (36.13%), suggesting an emerging conflict between human activities and landscape characteristics in this transition zone. In C2, both the $C \cap A$ and $A \cap L$ interactions exhibit a high degree of negative synergy, accounting for 41.13% and 38.71%, respectively. In contrast, the interaction between climate and landscape drivers ($C \cap L$) is characterized by a high degree of divergence (44.35%). This finding indicates that climatic and landscape factors often exert opposing directional effects, leading to significant uncertainty in the hydrological response. In C3, pairwise interactions among all three categories are predominantly positive synergies. Most notably, the interaction between anthropogenic and landscape drivers ($A \cap L$) reaches a positive contribution of 55.91%. This result implies that human activities and landscape characteristics increase the ω value.

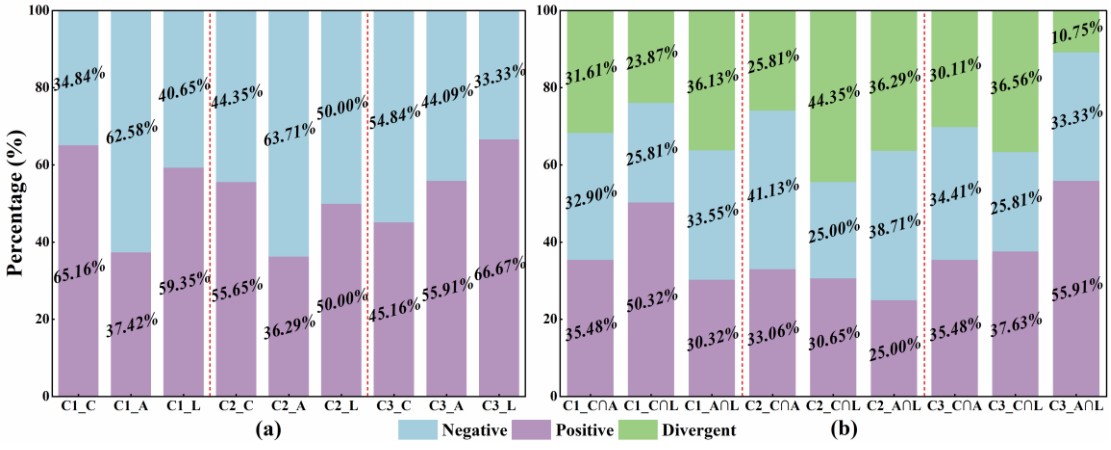

Figure 9: Directional consistency and interactive patterns of climatic, anthropogenic, and landscape drivers across the three zones. (a) Percentage of positive and negative contributions: The bars represent the proportion of samples where the aggregated SHAP values for climatic (C), anthropogenic (A), and landscape (L) drivers are positive (purple) or negative (blue). (b) Interaction patterns between driver categories: The bars illustrate the consistency of the directional impacts between pairs of driver categories (∩ denotes intersection). "Positive" (purple) indicates that both categories have positive SHAP sums; "negative" (blue) indicates that both have negative sums; and "divergent" (green) indicates that they have opposite signs (trade-off effects).

4 Discussion

4.1 Necessity of Functional Zoning

The fundamental premise of this study is that the 12 catchments, which span a vast climatic gradient, exhibit significant spatial heterogeneity in hydrological functioning (Blöschl, 2013; Beven, 2000). To verify whether a unified model could

https://doi.org/10.5194/egusphere-2026-969
Preprint. Discussion started: 26 February 2026

address this complexity, we first evaluated the performance of global machine learning models trained on the pooled dataset of all the catchments. Initially, the global models appeared to perform satisfactorily at an aggregate level. When evaluated on the pooled test set, the models generally achieved high accuracy, with overall R^2 values exceeding 0.9 and the RMSE remaining below 0.2. This result might suggest, misleadingly, that a single model is sufficient to capture the hydrological dynamics of the entire basin.

However, a deeper inspection of performance at the individual catchment level reveals the critical failure of this "one-size-fits-all" approach. As illustrated in Figure 10, we decomposed the global model performance to examine its stability across specific catchments. The boxplots reveal that despite the high median performance ($R^2 > 0.8$), there were significant outliers (black dots) where the model's predictive capability collapses (Gupta et al., 2014; Mizukami et al., 2017). For these specific catchments, R^2 decreased drastically to the range of 0.3–0.5, accompanied by a sharp increase in the RMSE. This finding indicates that while the global model captures the "average" behavior of the basin, it sacrifices accuracy in catchments with unique hydrological signatures that deviate from the mean. This failure indicates that a single global model cannot reconcile spatially nonstationary driving mechanisms across diverse regimes (Li et al., 2021; Berghuijs et al., 2014). Consequently, catchment classification becomes a prerequisite for disentangling such complexity (Wagener et al., 2007; Raux et al., 2011). Previous studies have emphasized that grouping catchments on the basis of similarity is essential for identifying distinct hydrological behaviors and reducing modeling uncertainty (Sawicz et al., 2014; Knoben et al., 2020). The sharp contrast between the "failure points" of the global model (Figure 10) and the consistently high accuracy of our cluster-based models (Figure 5) robustly validate the scientific necessity of the proposed objective functional zoning framework.

https://doi.org/10.5194/egusphere-2026-969
Preprint. Discussion started: 26 February 2026

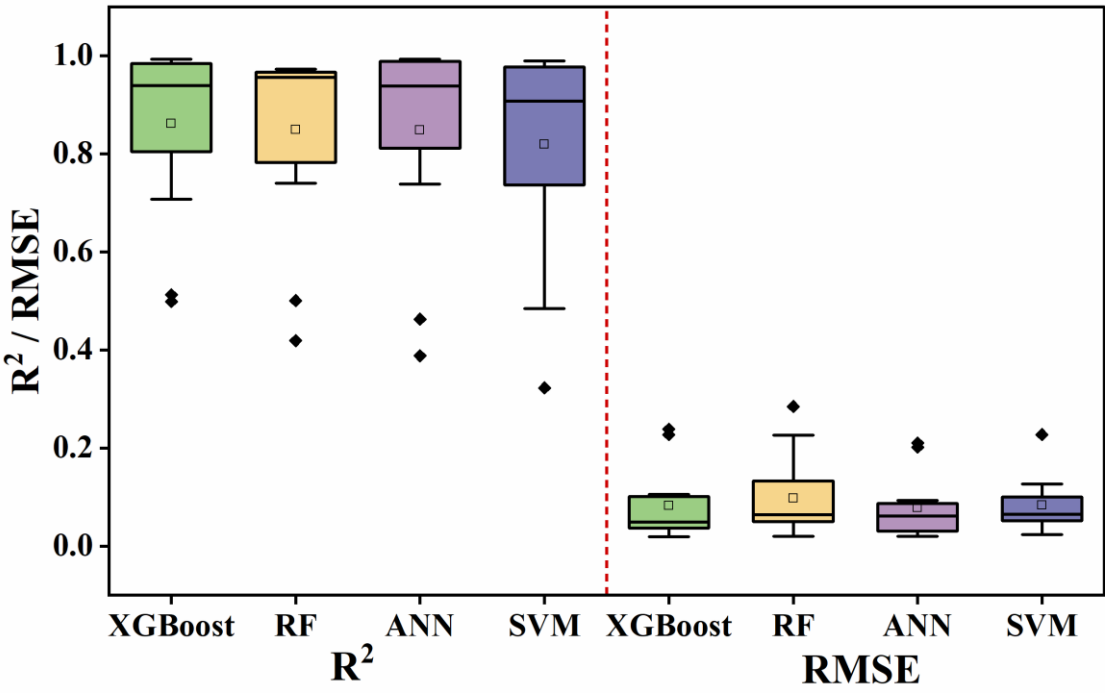

Figure 10: Distribution of performance of global machine learning models trained on the pooled dataset of all 12 catchments. The boxplots illustrate the variability in R^2 and RMSE for the four machine learning models when applied to the entire dataset without functional zoning. The black dots (outliers) highlight specific catchments where the global models failed significantly.

4.2 Shifting Dominance: From Natural Control to Anthropogenic Reconstruction

The quantitative attribution reveals a fundamental spatial transition in the drivers of catchment functioning across the 12 catchments spanning the semi-arid to semi-humid transition zone, depicting a trajectory from "nature-dominated" to "human-reconstructed" systems. C3 exhibits a "decoupling" of the hydrological cycle from natural climate variability. In this region, anthropogenic drivers explain 68.73% of the variation in ω, overwhelming climatic factors. A critical finding is the role of slope, which emerged as a dominant positive driver. Although slope is a static landscape feature, its positive contribution contradicts natural hydrological laws where steep terrains typically accelerate runoff (El Kateb et al., 2013). Here, slope acts as a spatial proxy for anthropogenic modification: soil conservation measures (e.g., terracing) are preferentially implemented on hillslopes exceeding specific gradients (as $> 15°$). These engineering structures effectively intercept runoff and convert it into soil water for evaporation (Ran et al., 2020; Liang et al., 2015). Combined with the positive influence of GDP (which reflects ecological investment to a certain extent), these findings suggest that human intervention has created a "physical buffer" that overrides natural topographic controls (Vörösmarty et al., 2004; Duarte et al., 2014). In contrast, climatic drivers account for the majority of feature importance (53.52%) in C1, confirming that hydrological processes in these high-altitude zones remain governed by classical Budyko boundary conditions, specifically

https://doi.org/10.5194/egusphere-2026-969
Preprint. Discussion started: 26 February 2026

energy availability (Yang et al., 2008; Budyko and Miller, 1974). This contrast highlights that without intensive landscape re-engineering, the basin's hydrology remains highly sensitive to natural climate fluctuations.

Uniquely, C2 exhibits a "tripartite balance", representing the complexity of the Anthropocene water cycle. The comparable contributions of climatic (37.24%), anthropogenic (31.85%), and landscape (30.91%) drivers suggest a system of tension and trade-off. Unlike the positive synergy in C3, anthropogenic factors in C2 (e.g., cropland and population) have a dominant negative effect on ω. These findings indicate that in developed plains, human activities function primarily through drainage acceleration (e.g., agricultural drainage systems and impervious surfaces) rather than retention (Blann et al., 2009; Shuster et al., 2005). This "hybrid" driving mechanism creates competing feedback between vegetation transpiration and human-induced drainage, clarifying the high instability observed in this region. Collectively, these findings demonstrate that the catchment parameter ω is not a static property but a dynamic outcome of local human–water coevolution (Di Baldassarre et al., 2019; Sivapalan et al., 2012).

4.3 Implications for Basin-Scale Water Resources Management

The identification of these three distinct regimes necessitates spatially differentiated management strategies. For C1, management should prioritize climate adaptation. Given the high sensitivity of ω to temperature ($T > 8.17\,^{\circ}C$; Figure 8), future warming may significantly accelerate evapotranspiration losses (Cuo et al., 2013). Therefore, strategies should focus on protecting natural vegetation (e.g., natural forests) to maintain soil water retention capacity and monitoring hydroclimatic feedbacks to ensure sustainable water yields for downstream areas (Barnett et al., 2005). For C2, the priority is to resolve the trade-off between development and water retention. The dominance of negative drivers like LAI and POP (Figure 8) suggests that both dense vegetation (likely agricultural) and urbanization accelerate water loss. Policies should promote water-saving agricultural practices to reduce drainage from high-LAI croplands, and implement low impact development or sponge city measures in urban areas (POP) to enhance local water retention and infiltration, counteracting the rapid runoff generation. (Xia et al., 2017; Kang et al., 2017). For C3, the focus must be on optimizing ecological engineering and controlling consumption. The strong positive contributions of GDP, $Slope$, and $Impervious$ confirm the effectiveness of ecological investments (e.g., terracing on steep slopes$>$ 8.8°,) and urban landscape management. However, the negative impact of WC and the declining marginal benefit of GDP at high levels warn of a resource ceiling. Management should shift from "construction" to "maintenance" of existing water conservation and strictly implement water withdrawal limits to prevent ecosystem degradation caused by water over-exploitation, avoiding the "threshold of unsustainability" (Fu et al., 2022; Feng et al., 2016).

4.4 Limitations and Future Perspectives

Despite the robust findings, several limitations of this study point to avenues for future research. First, data constraints limit the representation of deep hydrological processes. While we incorporated a comprehensive set of surface drivers, explicit

https://doi.org/10.5194/egusphere-2026-969
Preprint. Discussion started: 26 February 2026

data on groundwater dynamics and reservoir regulation rules were not included because of data unavailability at the basin scale. In regions such as C2, where groundwater extraction for irrigation is prevalent, this omission might contribute to relatively lower model stability. Future studies could integrate GRACE satellite data or localized groundwater monitoring to capture these subsurface signals (Tang et al., 2017). Second, the machine learning approach lacks physical process constraints. Although SHAP analysis provides interpretability, XGBoost remains a data-driven statistical model. It captures correlations rather than strict physical causality. As revealed by our preliminary experiments with spatial cross-validation (e.g., leave-one-basin-out schemes), the model's ability to extrapolate to unseen catchments is strictly constrained by the unique heterogeneity of each basin (Beven, 2020). A promising direction is the development of "physically guided machine learning" (PGML), which embeds physical laws (e.g., water balance constraints) into the loss function of machine learning models to improve both interpretability and generalizability (Karpatne et al., 2017; Reichstein et al., 2019). Third, the temporal scale of this study is annual. While the 11-year moving window effectively captures long-term trends, it masks out seasonal variability. However, seasonal mismatches between precipitation and vegetation growth (e.g., in the monsoon-dominated C1 zone) can significantly influence annual runoff (Fu and Wang, 2019; Yokoo et al., 2008). Future research should extend this diagnostic framework to monthly or daily scales to elucidate how intra-annual climate variability interacts with human activities to shape hydrological regimes.

5 Conclusions

In this study, a machine learning-driven diagnostic framework is proposed to determine the spatially divergent driving mechanisms of the Budyko parameter (ω) across the semi-arid to semi-humid transition zone. The parameter ω ranged from 1.74 to 3.79, indicating significant spatiotemporal heterogeneity and distinct distributional patterns. To better understand this complexity, we identified three hydrological functional zones using PCA and hierarchical clustering. Within these zones, the cluster-based XGBoost models consistently outperformed the RF, ANN, and SVM ($R^2 > 0.9$, $RMSE < 0.06$). This superior performance validates the robustness of the proposed framework in capturing regime-specific hydrological behaviors that global models often fail to resolve.

SHAP analysis revealed a fundamental spatial shift in the dominant drivers of ω across the three identified zones. C1 is driven primarily by climatic factors, which account for 53.52% of the total contribution, whereas C3 has transitioned to an anthropogenic-dominated regime, with human factors accounting for as much as 67.73%. Most notably, C2 exhibits a unique "tripartite balance," which is jointly driven by climatic (37.24%), anthropogenic (31.85%), and landscape (30.91%) factors. Specifically, T, LAI, and GDP were identified as the primary drivers for C1, C2, and C3, respectively. Beyond dominance ranking, the study quantified the distinct directional impacts and critical thresholds of these drivers. Systemically, climatic drivers exert a dominant positive contribution in C1 and C2 (accounting for >55%) but shift to a negative contribution in C3 (54.84%). In contrast, the directional impact of anthropogenic drivers is exactly opposite to that of climatic drivers in each zone. Landscape drivers mainly contribute positively to C1 and C3 but display a balanced split in C2 (50%). Furthermore,

https://doi.org/10.5194/egusphere-2026-969
Preprint. Discussion started: 26 February 2026

critical tipping points for the top-ranked drivers were identified: the positive (or negative) contributions of T, LAI, and GDP to ω are triggered at thresholds of 8.17 °C, 1.16, and 25.8×10^4 USD, respectively.

Finally, the analysis of pairwise interactions highlights the systemic complexity of human–water relations. Across all three zones, the interaction between climatic and anthropogenic drivers consistently manifests as a trade-off, distinguishing it from other interaction pairs. In contrast, C3 is characterized by a strong positive synergy between anthropogenic and landscape drivers, implying that human engineering and landscape modification act together to increase water retention. Collectively, these findings demonstrate that local landscape characteristics and human activity patterns can override macroclimatic controls, necessitating a shift from uniform management to spatially differentiated strategies for water resource sustainability.

Data availability

The daily meteorological data (precipitation and temperature) from 1980 to 2020 were obtained from the Climate Change Research Center (https://ccrc.iap.ac.cn/resource/detail?id=228). Potential evapotranspiration (E_0) was calculated using the standard Penman-Monteith equation, and the Aridity Index (AI) was derived as P/E_0. The observed monthly runoff data were acquired from the Yellow River Conservancy Commission, Ministry of Water Resources (http://www.yrcc.gov.cn/). The Digital Elevation Model data (30-meter resolution) were sourced from ASTER GDEM Version 3 (https://e4ftl01.cr.usgs.gov/ASTT/ASTGTM.003/) and used to calculate Slope and Elevation Coefficient of Variation (ECV).Crucially, to calculate the Available Water Storage Capacity ($AWSC$), we integrated soil hydraulic properties (plant available water content) from Zhang et al.(Zhang et al., 2018) (https://doi.org/10.1029/2018WR023539) with functional rooting depth data from Stocker et al. (Stocker et al., 2023) (https://doi.org/10.5281/zenodo.5515246). Leaf Area Index (LAI) data were sourced from the long-term 0.05° LAI dataset for China (https://doi.org/10.17605/OSF.IO/9QZ4K). Land use data were obtained from the Annual Land Cover Product of China (https://zenodo.org/records/8176941). Water consumption data (WC) were obtained from the High-resolution Sectoral Water Use Dataset (HSWUD) (https://doi.org/10.6084/m9.figshare.27610524). Socio-economic data were derived from high-resolution grid products: Population (POP) data were collected from the GlobPOP dataset (https://zenodo.org/records/11179644), and GDP data were obtained from the Global GDP raster dataset (https://doi.org/10.5281/zenodo.10976733). Both datasets were calibrated using Statistical Yearbooks of the relevant provinces.

Author contributions

BBD – conceptualization, data curation, formal analysis, investigation, resources, methodology, software, visualization, writing (original draft preparation). DDW – data curation, investigation, resources, supervision, validation, writing (review and editing). GDJ – conceptualization, data curation, funding acquisition, investigation, project administration, resources, supervision, writing (review and editing). XXY – conceptualization, data curation, funding acquisition, investigation, project

https://doi.org/10.5194/egusphere-2026-969
Preprint. Discussion started: 26 February 2026

administration, resources, supervision, writing (review and editing). YL – conceptualization, project administration, supervision, writing (review and editing).

Competing interests

The authors declare that they have no known competing financial interests or personal relationships that could have appeared to influence the work reported in this paper.

References

Barnett, T. P., Adam, J. C., and Lettenmaier, D. P.: Potential impacts of a warming climate on water availability in snow-dominated regions, Nature, 438, 303-309, https://doi.org/10.1038/nature04141, 2005.

Berghuijs, W. R., Sivapalan, M., Woods, R. A., and Savenije, H. H.: Patterns of similarity of seasonal water balances: A window into streamflow variability over a range of time scales, Water Resources Research, 50, 5638-5661, https://doi.org/10.1002/2014WR015692, 2014.

Beven, K. J.: Uniqueness of place and process representations in hydrological modelling, Hydrology and earth system sciences, 4, 203-213, https://doi.org/10.5194/hess-4-203-2000, 2000.

Beven, K. J.: A history of the concept of time of concentration, Hydrology and Earth System Sciences, 24, 2655-2670, https://doi.org/10.5194/hess-24-2655-2020, 2020.

Blann, K. L., Anderson, J. L., Sands, G. R., and Vondracek, B.: Effects of agricultural drainage on aquatic ecosystems: a review, Critical reviews in environmental science and technology, 39, 909-1001, https://doi.org/10.1080/10643380801977966, 2009.

Blöschl, G.: Runoff prediction in ungauged basins: synthesis across processes, places and scales, Cambridge University Press2013.

Budyko, M. I. and Miller, D. H.: Climate and life, 1974.

Choudhury, B.: Evaluation of an empirical equation for annual evaporation using field observations and results from a biophysical model, Journal of Hydrology, 216, 99-110, https://doi.org/10.1016/S0022-1694(98)00293-5, 1999.

Cuo, L., Zhang, Y. X., Gao, Y. H., Hao, Z. C., and Cairang, L. S.: The impacts of climate change and land cover/use transition on the hydrology in the upper Yellow River Basin, China, Journal Of Hydrology, 502, 37-52, https://doi.org/10.1016/j.jhydrol.2013.08.003, 2013.

Di Baldassarre, G., Sivapalan, M., Rusca, M., Cudennec, C., Garcia, M., Kreibich, H., Konar, M., Mondino, E., Mård, J., and Pande, S.: Sociohydrology: scientific challenges in addressing the sustainable development goals, Water Resources Research, 55, 6327-6355, https://doi.org/10.1029/2018WR023901, 2019.

Ding, B., Yu, X., and Jia, G.: Exploring the controlling factors of watershed streamflow variability using hydrological and machine learning models, Water Resources Research, 61, e2024WR039734, https://doi.org/10.1029/2024WR039734, 2025.

Duarte, R., Pinilla, V., and Serrano, A.: Looking backward to look forward: water use and economic growth from a long-term perspective, Applied Economics, 46, 212-224, https://doi.org/10.1080/00036846.2013.844329, 2014.

Duveiller, G., Hooker, J., and Cescatti, A.: The mark of vegetation change on Earth's surface energy balance, Nature communications, 9, 679, https://doi.org/10.1038/s41467-017-02810-8, 2018.

El Kateb, H., Zhang, H., Zhang, P., and Mosandl, R.: Soil erosion and surface runoff on different vegetation covers and slope gradients: A field experiment in Southern Shaanxi Province, China, Catena, 105, 1-10, https://doi.org/10.1016/j.catena.2012.12.012, 2013.

Feng, X., Fu, B., Piao, S., Wang, S., Ciais, P., Zeng, Z., Lü, Y., Zeng, Y., Li, Y., and Jiang, X.: Revegetation in China's Loess Plateau is approaching sustainable water resource limits, Nature Climate Change, 6, 1019-1022, 2016.

Fu, B.: On the calculation of the evaporation from land surface, Scientia Atmospherica Sinica, 5, 23, 1981.

Fu, B., Wu, X., Wang, Z., Wu, X., and Wang, S.: Coupling human and natural systems for sustainability: Experiences from China's Loess Plateau, Earth System Dynamics Discussions, 2022, 1-22, https://doi.org/10.5194/esd-13-795-2022, 2022.
Fu, J. and Wang, W.: On the lower bound of Budyko curve: The influence of precipitation seasonality, Journal of Hydrology, 570, 292-303, https://doi.org/10.1016/j.jhydrol.2018.12.062, 2019.
Gupta, H. V., Perrin, C., Blöschl, G., Montanari, A., Kumar, R., Clark, M., and Andréassian, V.: Large-sample hydrology: a need to balance depth with breadth, Hydrology And Earth System Sciences, 18, 463-477, 10.5194/hess-18-463-2014, 2014.
Huang, J., Yu, H., Guan, X., Wang, G., and Guo, R.: Accelerated dryland expansion under climate change, Nature climate change, 6, 166-171, https://doi.org/10.1038/nclimate2837, 2016.
Kang, S., Hao, X., Du, T., Tong, L., Su, X., Lu, H., Li, X., Huo, Z., Li, S., and Ding, R.: Improving agricultural water productivity to ensure food security in China under changing environment: From research to practice, Agricultural Water Management, 179, 5-17, https://doi.org/10.1016/j.agwat.2016.05.007, 2017.
Karpatne, A., Atluri, G., Faghmous, J. H., Steinbach, M., Banerjee, A., Ganguly, A., Shekhar, S., Samatova, N., and Kumar, V.: Theory-guided data science: A new paradigm for scientific discovery from data, IEEE Transactions on knowledge and data engineering, 29, 2318-2331, https://doi.org/10.1109/TKDE.2017.2720168, 2017.
Knoben, W. J., Freer, J. E., Peel, M., Fowler, K., and Woods, R. A.: A brief analysis of conceptual model structure uncertainty using 36 models and 559 catchments, Water Resources Research, 56, e2019WR025975, https://doi.org/10.1029/2019WR025975, 2020.
Koster, R. D., Dirmeyer, P. A., Guo, Z., Bonan, G., Chan, E., Cox, P., Gordon, C., Kanae, S., Kowalczyk, E., and Lawrence, D.: Regions of strong coupling between soil moisture and precipitation, Science, 305, 1138-1140, https://doi.org/10.1126/science.1100217, 2004.
Li, H., Shi, C., Sun, P., Zhang, Y., and Collins, A. L.: Attribution of runoff changes in the main tributaries of the middle Yellow River, China, based on the Budyko model with a time-varying parameter, Catena, 206, 105557, https://doi.org/10.1016/j.catena.2021.105557, 2021.
Liang, W., Bai, D., Wang, F., Fu, B., Yan, J., Wang, S., Yang, Y., Long, D., and Feng, M.: Quantifying the impacts of climate change and ecological restoration on streamflow changes based on a B udyko hydrological model in China's Loess Plateau, Water Resources Research, 51, 6500-6519, https://doi.org/10.1002/2014WR016589, 2015.
Lundberg, S. M. and Lee, S.-I.: A unified approach to interpreting model predictions, Advances in neural information processing systems, 30, 2017.
Milly, P. C., Betancourt, J., Falkenmark, M., Hirsch, R. M., Kundzewicz, Z. W., Lettenmaier, D. P., and Stouffer, R. J.: Stationarity is dead: Whither water management?, Science, 319, 573-574, https://doi.org/10.1126/science.1151915, 2008.
Mizukami, N., Clark, M. P., Newman, A. J., Wood, A. W., Gutmann, E. D., Nijssen, B., Rakovec, O., and Samaniego, L.: Towards seamless large-domain parameter estimation for hydrologic models, Water Resources Research, 53, 8020-8040, https://doi.org/10.1002/2017WR020401, 2017.
Murdoch, W. J., Singh, C., Kumbier, K., Abbasi-Asl, R., and Yu, B.: Definitions, methods, and applications in interpretable machine learning, Proceedings of the National Academy of Sciences, 116, 22071-22080, https://doi.org/10.1073/pnas.1900654116, 2019.
Ni, Y., Yu, Z., Lv, X., Qin, T., Yan, D., Zhang, Q., and Ma, L.: Spatial difference analysis of the runoff evolution attribution in the Yellow River Basin, Journal of Hydrology, 612, 128149, https://doi.org/10.1016/j.jhydrol.2022.128149, 2022.
Oudin, L., Andréassian, V., Perrin, C., Michel, C., and Le Moine, N.: Spatial proximity, physical similarity and ungaged catchments: confrontation on 913 French catchments, Water Resources Research, 44, W03413, 2008.
Papacharalampous, G., Tyralis, H., and Koutsoyiannis, D.: Comparison of stochastic and machine learning methods for multi-step ahead forecasting of hydrological processes, Stochastic environmental research and risk assessment, 33, 481-514, https://doi.org/10.1007/s00477-018-1638-6, 2019.
Peng, K., Zhang, Y., Tang, Q., Zhang, Y., Li, Z., Wang, G., and Cao, C.: Decomposing the effects of changes in catchment characteristics on runoff into chain transmission effects of climate change and human activities using an improved Budyko framework, Earth's Future, 13, e2025EF006041, https://doi.org/10.1029/2025EF006041, 2025.
Rajib, M. A., Merwade, V., Kim, I. L., Zhao, L., Song, C., and Zhe, S.: SWATShare–A web platform for collaborative research and education through online sharing, simulation and visualization of SWAT models, Environmental Modelling & Software, 75, 498-512, https://doi.org/10.1016/j.envsoft.2015.10.032, 2016.

https://doi.org/10.5194/egusphere-2026-969
Preprint. Discussion started: 26 February 2026

Ran, Q., Chen, X., Hong, Y., Ye, S., and Gao, J.: Impacts of terracing on hydrological processes: A case study from the Loess Plateau of China, Journal of Hydrology, 588, 125045, https://doi.org/10.1016/j.jhydrol.2020.125045, 2020.

Raux, J., Copard, Y., Laignel, B., Fournier, M., and Masseï, N.: Classification of worldwide drainage basins through the multivariate analysis of variables controlling their hydrosedimentary response, Global and Planetary Change, 76, 117-127, https://doi.org/10.1016/j.gloplacha.2010.12.005, 2011.

Reichstein, M., Camps-Valls, G., Stevens, B., Jung, M., Denzler, J., Carvalhais, N., and Prabhat, F.: Deep learning and process understanding for data-driven Earth system science, Nature, 566, 195-204, https://doi.org/10.1038/s41586-019-0912-1, 2019.

Sawicz, K., Wagener, T., Sivapalan, M., Troch, P. A., and Carrillo, G.: Catchment classification: empirical analysis of hydrologic similarity based on catchment function in the eastern USA, Hydrology and Earth System Sciences, 15, 2895-2911, https://doi.org/10.5194/hess-15-2895-2011, 2011.

Sawicz, K., Kelleher, C., Wagener, T., Troch, P., Sivapalan, M., and Carrillo, G.: Characterizing hydrologic change through catchment classification, Hydrology and Earth System Sciences, 18, 273-285, https://doi.org/10.5194/hess-18-273-2014, 2014.

Seneviratne, S. I., Corti, T., Davin, E. L., Hirschi, M., Jaeger, E. B., Lehner, I., Orlowsky, B., and Teuling, A. J.: Investigating soil moisture–climate interactions in a changing climate: A review, Earth-Science Reviews, 99, 125-161, https://doi.org/10.1016/j.earscirev.2010.02.004, 2010.

Shen, C.: A transdisciplinary review of deep learning research and its relevance for water resources scientists, Water Resources Research, 54, 8558-8593, https://doi.org/10.1029/2018WR022643, 2018.

Shen, Q., Cong, Z., and Lei, H.: Evaluating the impact of climate and underlying surface change on runoff within the Budyko framework: A study across 224 catchments in China, Journal of Hydrology, 554, 251-262, https://doi.org/10.1016/j.jhydrol.2017.09.023, 2017.

Shortridge, J. E., Guikema, S. D., and Zaitchik, B. F.: Machine learning methods for empirical streamflow simulation: a comparison of model accuracy, interpretability, and uncertainty in seasonal watersheds, Hydrology and Earth System Sciences, 20, 2611-2628, https://doi.org/10.5194/hess-20-2611-2016, 2016.

Shuster, W. D., Bonta, J., Thurston, H., Warnemuende, E., and Smith, D. R.: Impacts of impervious surface on watershed hydrology: A review, Urban Water Journal, 2, 263-275, https://doi.org/10.1080/15730620500386529, 2005.

Sit, M., Demiray, B. Z., Xiang, Z., Ewing, G. J., Sermet, Y., and Demir, I.: A comprehensive review of deep learning applications in hydrology and water resources, Water Science and Technology, 82, 2635-2670, https://doi.org/10.2166/wst.2020.369, 2020.

Sivapalan, M.: Prediction in ungauged basins: a grand challenge for theoretical hydrology, https://doi.org/10.1002/hyp.8426, 2003.

Sivapalan, M., Savenije, H. H., and Blöschl, G.: Socio-hydrology: A new science of people and water, Hydrological Processes, 26, 1270-1276, https://doi.org/10.1002/hyp.8426, 2012.

Stocker, B. D., Tumber-Dávila, S. J., Konings, A. G., Anderson, M. C., Hain, C., and Jackson, R. B.: Global patterns of water storage in the rooting zones of vegetation, Nature geoscience, 16, 250-256, https://doi.org/10.1038/s41561-023-01125-2, 2023.

Tang, Y., Hooshyar, M., Zhu, T., Ringler, C., Sun, A. Y., Long, D., and Wang, D.: Reconstructing annual groundwater storage changes in a large-scale irrigation region using GRACE data and Budyko model, Journal of Hydrology, 551, 397-406, https://doi.org/10.1016/j.jhydrol.2017.06.021, 2017.

Troch, P. A., Lahmers, T., Meira, A., Mukherjee, R., Pedersen, J. W., Roy, T., and Valdés-Pineda, R.: Catchment coevolution: A useful framework for improving predictions of hydrological change?, Water Resources Research, 51, 4903-4922, https://doi.org/10.1002/2015WR017032, 2015.

Vörösmarty, C., Lettenmaier, D., Leveque, C., Meybeck, M., Pahl-Wostl, C., Alcamo, J., Cosgrove, W., Grassl, H., Hoff, H., and Kabat, P.: Humans transforming the global water system, Eos, Transactions American Geophysical Union, 85, 509-514, https://doi.org/10.1029/2004EO480001, 2004.

Wagener, T., Sivapalan, M., Troch, P., and Woods, R.: Catchment classification and hydrologic similarity, Geography compass, 1, 901-931, https://doi.org/10.1111/j.1749-8198.2007.00039.x, 2007.

https://doi.org/10.5194/egusphere-2026-969
Preprint. Discussion started: 26 February 2026

Xia, J., Zhang, Y., Xiong, L., He, S., Wang, L., and Yu, Z.: Opportunities and challenges of the Sponge City construction related to urban water issues in China, Science China Earth Sciences, 60, 652-658, https://doi.org/10.1007/s11430-016-0111-8, 2017.

Xu, X., Yang, D., Yang, H., and Lei, H.: Attribution analysis based on the Budyko hypothesis for detecting the dominant cause of runoff decline in Haihe basin, Journal of Hydrology, 510, 530-540, https://doi.org/10.1016/j.jhydrol.2013.12.052, 2014.

Yang, H., Yang, D., and Hu, Q.: An error analysis of the Budyko hypothesis for assessing the contribution of climate change to runoff, Water Resources Research, 50, 9620-9629, https://doi.org/10.1002/2014WR015451, 2014.

Yang, H., Yang, D., Lei, Z., and Sun, F.: New analytical derivation of the mean annual water-energy balance equation, Water resources research, 44, https://doi.org/10.1029/2007WR006135, 2008.

Yin, J., He, F., Xiong, Y. J., and Qiu, G. Y.: Effects of land use/land cover and climate changes on surface runoff in a semi-humid and semi-arid transition zone in northwest China, Hydrology and Earth System Sciences, 21, 183-196, https://doi.org/10.5194/hess-21-183-2017, 2017.

Yokoo, Y., Sivapalan, M., and Oki, T.: Investigating the roles of climate seasonality and landscape characteristics on mean annual and monthly water balances, Journal of Hydrology, 357, 255-269, https://doi.org/10.1016/j.jhydrol.2008.05.010, 2008.

Zhai, R. and Tao, F. L.: Contributions of climate change and human activities to runoff change in seven typical catchments across China, Science Of the Total Environment, 605, 219-229, https://doi.org/10.1016/j.scitotenv.2017.06.210, 2017.

Zhang, L., Dawes, W., and Walker, G.: Response of mean annual evapotranspiration to vegetation changes at catchment scale, Water resources research, 37, 701-708, https://doi.org/10.1029/2000WR900325, 2001.

Zhang, L., Hickel, K., Dawes, W., Chiew, F. H., Western, A., and Briggs, P.: A rational function approach for estimating mean annual evapotranspiration, Water resources research, 40, https://doi.org/10.1029/2003WR002710, 2004.

Zhang, Y., Schaap, M. G., and Zha, Y.: A high-resolution global map of soil hydraulic properties produced by a hierarchical parameterization of a physically based water retention model, Water Resources Research, 54, 9774-9790, https://doi.org/10.1029/2018WR023539, 2018.